Energy Conversion and Management 132 (2017) 221–230

ASSESMENT OF COMPRESSIBILITY EFFECTS ON INTERNAL NOZZLE FLOW IN DIESEL INJECTORS AT VERY HIGH INJECTION PRESSURES

Salvador, F.J. (*)[1], De la Morena, J.[1], Martínez-López, J.[2] , Jaramillo, D.[1]

[1] CMT-Motores Térmicos. Universitat Politècnica de València, Spain

[2] Williams Grand Prix Engineering Limited, United Kingdom

(*) Corresponding author:

Dr. F. Javier Salvador, fsalvado@mot.upv.es

CMT-Motores Térmicos, Universitat Politècnica de València

Camino de Vera s/n, E-46022 Spain.

Telephone: +34-963879658

FAX: +34-963877659

ABSTRACT

Diesel fuel injection systems are being used at higher injection pressure conditions over time because of more stringent emissions requirements. Thus, the importance to properly take into account the fluid compressibility on injection CFD simulations is also increasing. In this paper, an investigation of the compressibility effects in nozzle flow simulations has been carried out for injection pressures up to 250 MPa. To do so, the fluid properties (including density, viscosity and speed of sound) have been measured in a wide range of boundary conditions. These measurements have allowed to obtain correlations for the fluid properties as a function of pressure and temperature. Then, these equations have been incorporated to a CFD solver to take into account the variation of the fluid properties with the pressure changes along the computational domain. The results from

these simulations have been compared to experimental mass flow rate and momentum flux results, showing a significant increase in accuracy with respect to an incompressible flow solution.

KEYWORDS: nozzle, modelling, Diesel, dynamic, compressibility, CFD

NOMENCLATURE

a_f	Fuel speed of sound
A_o	Geometrical nozzle outlet area
C_d	Discharge coefficient, $C_d = \frac{\dot{m}}{\rho_f \cdot A_o \cdot u_b}$
D_i	Geometrical nozzle inlet diameter
D_o	Geometrical nozzle outlet diameter
k-factor	Nozzle conicity, $k - factor = \frac{D_i[\mu m] - D_o[\mu m]}{10}$
$\dot{m}$	Mass flow
$\dot{M}$	Momentum flux,
P	Fluid pressure
P_b	Discharge pressure
P_{inj}	Injection pressure
T	Fluid temperature

u_{eff} Effective outlet nozzle orifice velocity

u_b Theoretical outlet orifice velocity, $u_b = \sqrt{\dfrac{2 \cdot (P_{inj} - P_b)}{\rho_f}}$

Greek Symbols

ΔP Pressure drop, $\Delta P = P_{inj} - P_b$

ρ_f Fuel density

υ_f Kinematic viscosity

μ_f Dynamic viscosity

μ_0 Dynamic viscosity at 0.1MPa pressure

1. INTRODUCTION.

In the last decades, diesel engine researchers have focused on minimizing the exhaust emissions maintaining the thermal efficiency advantage compared to gasoline engines. In particular, efforts have been made to achieve a combined reduction of nitrogen oxides and soot particles, which are characteristic of the lean diffusive combustion process existing in such engines [1], [2].

Two main paths have been followed to reduce exhaust emissions in diesel engines. On the one hand, several aftertreatment components, such as Diesel Particulate Filter (DPF), Diesel Oxidation Catalyst (DOC), Selective Catalyst Reduction (SCR) or Lean-NOx Trap (LNT) have been placed at the engine outlet to collect and/or convert the exhaust emissions before reaching the atmosphere [3], [4]. On the other hand, new combustion modes with high levels of Exhaust Gas Recirculation (EGR) and higher rates of premixed combustion have been implemented to reduce the emissions at engine-out [5]–[8]. The performance of the fuel injection system has been proven as critical for such strategies, since it controls the atomization and fuel-air mixing processes [9]–[11].

Many authors have tried to study the characteristics of the flow inside the fuel injector, and in particular inside the nozzle orifices. Several studies have made use of transparent geometries for this purpose, but many of them explored simplified geometries [12]–[15] or were significantly limited in the maximum achievable injection pressure [16]–[18]. Thus, Computational Fluid Dynamics (CFD) tools have been developed on the last decades as a tool to get further insight in the relationship between the nozzle geometry, the internal flow characteristics and the hydraulic conditions at the nozzle exit [19]–[22], which are a necessary input for spray combustion models [23]–[26].

The fuel physical properties (mainly density and viscosity) have a significant impact on the internal nozzle flow characteristics. Battistoni et al [23] compared the internal flow and near-nozzle spray details for a standard diesel fuel and a soybean methyl ester (SME), showing that the different viscosity among them severely impacts both the outlet mass flow rate and the spray features. Similar conclusions about the effect of the fuel properties have already been seen both experimentally and numerically for other kinds of biodiesel [27]–[31] and for winter fuel formulations [32]–[34]. Recently, a few authors [35]–[39] have showed that it is important to consider not only the changes in the fuel properties related to the fuel composition, but also those related to the different temperature and pressure conditions along the nozzle geometry, which are traditionally neglected.

In the current paper, an effort to understand the impact of compressibility effects on internal nozzle flow simulations at very high injection pressure (up to 250 MPa) has been performed. For this purpose, the fuel used for the study has been widely characterized at different levels of temperature and pressure, producing the corresponding correlations for the fuel density, viscosity and speed of sound. Then, the hydraulic behavior of the injector has been determined in terms of injection rate and momentum flux for different levels of injection pressure and backpressure. These results have been finally compared to internal flow CFD simulations carried out with two strategies: constant fuel properties (incompressible) and pressure-dependent fuel properties (compressible). This procedure allows to quantify the differences obtained in the main flow parameters when compressibility effects are considered compared to the more simple incompressible solution generally seen in the literature [15], [40], [41].

The paper is structured in 5 sections. In section 2, the main experimental methodologies used along the study are described, together with the correlations obtained for the main fuel physical properties. Section 3 details the setup used for the internal flow CFD study, whose main results are depicted in Section 4. Finally, the main conclusions obtained from the work are drawn in Section 5.

2. EXPERIMENTAL TOOLS

In this section, the main experimental techniques used for the study are briefly described.

2.1. Nozzle geometry determination

For the current study, a solenoid-driven diesel injector with a 5-orifices convergent nozzle has been used. In order to perform the internal nozzle flow simulations, it is necessary to have all its geometrical details. To do so, a previously developed and validated silicone molding technique has been employed. The technique is based on the injection of the silicone on a semi-liquid state into the nozzle, once the needle has been removed. After a few hours, the silicone becomes solid and can be extracted, maintaining the internal geometry of the sac and the orifices. The mold is later inspected using a Scanning Electron Microscope, determining the corresponding nozzle dimensions.

An example of the pictures obtained through this process can be seen in Figure 1, while more details on the experimental technique are available in [42]. Finally, the final geometrical values of the nozzle used for the study can be seen in Table 1. In this table, R_a and R_b are the rounding radii at the orifice inlet in the upper and lower side of the orifice, respectively; D_i, D_o and D_m are the diameters in the inlet, outlet and middle sections of the orifices; and *k-factor* is a parameter related to the nozzle orifice conicity, defined as:

$$k-factor = \frac{D_i[\mu m] - D_o[\mu m]}{10} \quad (1)$$

Since the nozzle orifices are significantly convergent (as it can be seen from its high value of *k-factor*), low probability of cavitation formation inside the nozzle is expected [43], [44]. Nevertheless, some cavitation could appear when very high injection pressures are used. This will be further analyzed in Section 4.

2.2. Fuel properties characterization

As a first step, the main physical properties of the fuel have been measured under a wide range of pressure and temperature conditions. In particular, a standard European winter diesel fuel has been used. Density measurements were performed on a hydrometer, based on the ASTMD1298 procedure, while a standard viscometer was used to characterize the fuel viscosity. Finally, a custom-made facility was constructed to characterize the speed of sound. This facility was based on a standard common-rail system, onto which a long tube has been installed between the rail and the injector. On that line, two high-speed piezoelectric pressure transducers have been installed at two different positions. Once the injector is commanded and the injection event takes place, a pressure wave is generated inside the system. Knowing the distance between these two transducers, it is possible to characterize the speed of sound by measuring the time lapse that the pressure perturbation takes to travel to one sensor to another. More information about the experimental setup can be seen in [45].

Figure 2 shows the results from the fuel characterization for a range of 0.1-300 MPa in pressure and 300-400 K in temperature, which are representative of the usage of diesel fuel in advanced common rail systems. These data have been correlated as a function of pressure and temperature, finding the following relationships:

$$\begin{aligned}\rho_f &= 826.5 - 1.0217(T-298) + 1.251\cdot 10^{-3}(T-298)^2 + 0.6035(P-0.1) \\ &- 8.27\cdot 10^{-4}(P-0.1)^2 + 1.44\cdot 10^{-3}(P-0.1)(T-298)\end{aligned} \tag{2}$$

$$\mu_f = 10^{-3}\mu_0 \cdot 10^{\left[\left(-1.48+5.86\mu_0^{0.181}\right)\cdot\left(\frac{P-0.1013}{1000}\right)\right]} \tag{3}$$

$$\mu_0 = 3.2158\cdot\exp\left[0.0263(T-298)\right] \tag{4}$$

$$\begin{aligned}a_f &= 1350.6 - 3.1485(T-298) + 4.4928(P-0.1) - 6.96\cdot 10^{-3}(P-0.1)^2 \\ &+ 7.4\cdot 10^{-3}(P-0.1)(T-298)\end{aligned} \tag{5}$$

Where ρ_f is the fuel density in kg/m^3, μ_f is the fuel dynamic viscosity in Pa·s, μ_0 is the fuel dynamic viscosity at 0.1 MPa of pressure, a_f is the speed of sound of the fuel in m/s, P is the fuel pressure in MPa and T is the fuel temperature in K.

2.3. Injection rate meter

An IAV injection rate meter has allowed to determine the instantaneous mass flow rate delivered by the injector at different boundary conditions, summarized in Table 2. The technique is based on the Bosch method [46], which relates the instantaneous injected quantity to the pressure increase on a tube placed at the injector outlet. More details on the experimental arrangement and postprocessing procedure can be found in [47].

Figure 3 shows an example of the results obtained for a particular case of 180 MPa injection pressure (P_{inj}), 2 ms of energizing time (*ET*) and different levels of backpressure (P_b). The curve represents the instantaneous mass flow injected by the combination of the 5 nozzle orifices. As it is usual for the high injection pressure cases, the effect of the backpressure is only appreciable on the steady-state phase of the injection event. During this region, the mass flow rate through the nozzle corresponds to the following expression:

$$\dot{m} = C_d \rho_f A_o u_b = C_d A_o \sqrt{2\left(P_{inj} - P_b\right)\rho_f} \tag{6}$$

Where $\dot{m}$ is the mass flow rate through the nozzle, C_d is the discharge coefficient of the nozzle, A_o is the geometrical outlet area of the nozzle orifices and u_b is the theoretical nozzle outlet velocity according to Bernoulli's equation. According to this expression, and as it can be seen in Figure 3, higher backpressure values correspond to lower stationary mass flow rates.

2.4. Momentum flux test rig

A dedicated test rig has allowed to obtain the momentum of the sprays produced by the injector. In this rig, the fuel is injected on chamber filled with an inert pressure gas (nitrogen in this case). A compound of a piezoelectric pressure transducer and a target is placed perpendicular to one of the orifices of the fuel injector, at a distance of 5 mm. The transducer is properly calibrated so that it can measure the impact force of the spray into the target, which is then transmitted to the transducer. More details of the technique can be found in [48]. The experimental matrix for the momentum flux measurements, which is a subset of the one already seen for the injection rate meter, is available in Table 3. In this case, the maximum backpressure was limited to 7 MPa due to structural limitations of the test rig.

Figure 4 shows a schematic of the momentum flux experimental arrangement, together with an example of the results again for the P_{inj}=180 MPa case. The results seen in the figure are an average of the data coming from the 5 nozzle orifices.

3. NUMERICAL SETUP

Internal nozzle flow simulations have been carried out using a single-phase isothermal flow solver in ANSYS ® Fluent ® v.17 [49]. Regarding the turbulence model, Re-Normalization Group (RNG) k-ε model has been selected based on previous internal flow simulation experiences [41], [50]. The geometry has been simplified to a 72º sector-mesh, corresponding to a single nozzle orifice, in order to minimize the computational effort. The mean orifice dimensions included in Table 2 have been used for this purpose.

Figure 5 shows the computational domain with a detail of the mesh structure in the orifice. Constant pressure boundary condition is selected for the Inlet and Outlet boundary conditions, with values equal to the experimental data at the fuel injector inlet and outlet during the injection rate experimental campaign. Non-slip boundary condition is used for the nozzle and needle walls.

Figure 6 shows the results for a mesh sensitivity study and the comparison between first and second order numerical schemes. This has been performed for an injection pressure of 130 MPa and a backpressure of 7 MPa. The fuel properties (density and viscosity) have been considered constant along the whole computational domain (incompressible solution). From Figure 6, it can be observed that second order schemes reach the mesh independence for a relatively small number of cells (#208000), while first order numerical schemes do not show mesh convergence for significantly higher number of cells (#272000). Thus, in order to minimize the computational effort of the simulations, second order schemes with the 208000 cells configuration have been selected for the study. This configuration leads to an overestimation in the experimental mass flow rate of approximately 5.5%.

Using the previously determined mesh characteristics, all cases presented in Table 2 have been run on a single processor Intel (R) Core (TM) i5-4460 CPU @ 3.20 GHz. The simulations have been run on a steady-state solver, using two main convergence criteria: first, all the residuals must be below 5·10-5; additionally, the average velocity at the nozzle orifice outlet must reach stationary conditions with 1% tolerance. The simulations are initialized with injection pressure and zero velocity in the internal fluid domain. Doing so, and for the particular case of an injection pressure of 130 MPa and a backpressure of 5 MPa, the incompressible solver reaches convergence after 1778 iterations, leading to a total CPU time of 2421.7 seconds. For the same conditions, the compressible approach takes 1860 iterations and 3059.9 seconds to converge, which represents an increase of the computational effort of approximately 26%. Similar results on a relative basis are obtained for other operating conditions.”

4. INTERNAL FLOW SIMULATION RESULTS

In the current section, internal nozzle flow simulation results will be analyzed comparing two different strategies. First, the fuel properties are considered constant for the whole computational domain. For this purpose, density and viscosity are calculated at the backpressure condition. Then, the equations described in Section 2 for the density, viscosity and speed of sound of the fuel are introduced into the solver by means of user-defined functions, in order to account for the fuel compressibility. For both cases, the flow is considered isothermal with a temperature level of 298 K, which is the value existing at the fuel injector inlet during the experimental injection rate and momentum flux measurements.

Figure 7 shows an example of the density and viscosity fields inside the nozzle for the compressible configuration. As a consequence of the pressure evolution inside the nozzle, which will be later analyzed in Figure 8, the compressible solver estimates a variation of around 100 kg/m^3 in density and of around $8 \cdot 10^{-2}$ kg/m·s in dynamic viscosity along the computational domain. These variations have a double impact: on the one hand, the variations in the fuel properties are expected to induce significant changes in the nozzle outlet velocity and mass flow rate compared to the incompressible solution, as it will analyzed in the next paragraphs; on the other hand, the variations of viscosity affect the local Reynolds number, with consequences in the turbulent flow characteristics.

Figure 8 shows the comparison of pressure and velocity fields for the compressible and incompressible solvers for the same condition analyzed in Figure 7. One of the first things that can be highlighted is that even for this very high injection pressure, the minimum computed pressure values inside the nozzle orifices (around 0.5 MPa) are always higher than the fuel saturation pressure. This means that this particular geometry would not produce any cavitation thanks to the combination of high conicity and relatively high rounding radii. Another significant difference is seen in the velocity fields. In the compressible solution, higher fuel viscosity values are observed compared to the incompressible approach, where the viscosity is calculated at backpressure conditions. For this reason, higher viscous dissipation appears, leading to lower velocities. This can be easily perceived looking at the maximum velocity along the computational domain, which is around 58 m/s lower for the compressible case. Additionally, both pressure and velocity contours show smoother transitions along the computational domain when including the flow compressibility effects.

The impact of the variation of the properties inside the nozzle over the hydraulic behavior of the nozzle can be clearly observed in Figure 9. This figure compares the experimental mass flow at the nozzle outlet with the simulation results obtained with and without the compressibility equations enabled. In the case of the experimental results, the data corresponds to a time average of the injection rate during its steady-state phase, where the mass flow is not affected by the needle position, as it was introduced in Section 2. In these results, the simulations tend to overestimate the mass flow for all conditions. At relatively low injection pressures (30 MPa), the solution given by the compressible and incompressible approaches are relatively similar, since the range of variation of the fluid properties is moderate. However, it is appreciable that the compressible solution is closer to the experimental values, as it is more capable of representing the flow physics. As the injection pressure increases, the compressible and incompressible solutions diverge, reaching a maximum difference of approximately 5% in mass flow at the maximum injection pressure tested (250 MPa).

Figure 10 shows the evolution of the discharge coefficient against the square root of the pressure drop for both compressible and incompressible flow, together with the experimental values. For all of them it can be seen how the discharge coefficient is highly dependent on the pressure drop along the nozzle at low $\Delta P^{1/2}$ conditions, while the dependence is much smaller as the pressure drop increases. This behavior is due to the impact of the flow regime on the discharge coefficient. At low injection pressures, flow velocities are moderate and the flow is in transitional conditions between laminar and turbulent, for which the discharge coefficient is highly sensitive to the Reynolds number. As the injection pressure increase, so does the velocity, the flow regime becomes fully turbulent and the discharge coefficient is independent on the Reynolds number. Similar behavior has been repeatedly found in the literature for different orifice geometries [51]–[53]

Regarding the effect of compressibility, at low injection pressures both approaches clearly overestimate the discharge coefficient, although the compressible solution gives better results. The relatively high difference between model an experiments at these conditions may be due to uncertainties in aspects such as the nozzle geometry or the turbulence model. As the injection pressure increases, the importance of the flow compressibility ramps up, the compressible and incompressible solutions diverge, and it is clearly seen how the compressible flow solver is more capable to reproduce the experimental data, while the incompressible solver maintains a deviation of approximately 0.08 in the absolute value of the discharge coefficient.

Figure 11 plots the hydraulic performance of the nozzle in terms of its effective outlet velocity, calculated as the ratio between the momentum flux and the mass flow. For the experiments, the time-averaged values at the steady-state phases of the injection rate and momentum flux curves are considered. For the CFD calculations, the mass flow and momentum flux values are integrated in the nozzle outlet section. It can be observed that the incompressible solution overestimates again the outlet velocity, while the values obtained using the compressible flow approach are very similar to the experiments for all the conditions tested.

Finally, Figures 12 and 13 show the mass flow and effective outlet velocity results expressed as the percentage deviation to the experimental data. In both cases, it can be seen how this deviation tends to reduce when increasing the injection pressure. Comparing the two simulation approaches, the compressible flow solution is around 5% closer to the experiments in terms of mass flow. This fact points out the importance of an accurate reproduction of the fluid properties when trying to reproduce the hydraulic behavior of a nozzle through simulations. Regarding the effective velocity, the results pass from around 3% of overestimation in the high-pressure range for the incompressible simulation to a 1% underestimation in the case of the compressible solution, while the deviations are significantly higher for the constant-properties approach.

5. CONCLUSIONS.

In the current paper, an investigation of the compressibility effects on diesel nozzle internal flow simulations has been performed. First, the fluid density, viscosity and speed of sound have been characterized as a function of pressure and temperature on a wide range of boundary conditions. Correlations of these properties have been estimated and then implemented on ANSYS ® Fluent ® v.17. Later, the hydraulic behavior of a 5-orifices convergent nozzle has been characterized by means of mass flow rate and momentum flux experimental tests, exploring values of injection pressure up to 250 MPa. From these results, the evolution of the mass flow rate, momentum flux and effective outlet velocity at maximum lift conditions have been extracted. Then, these values are compared to steady-state CFD simulations at two conditions:

- Incompressible flow: constant fluid properties.
- Compressible flow: fluid properties locally computed as a function of the flow pressure conditions.

The results from the compressible flow simulations show a variation of around 100 kg/m^3 in density and of around $8\cdot10^{-2}$ kg/m·s in dynamic viscosity along the nozzle geometry. This implies a significant reduction of the uncertainties related to internal nozzle flow simulations without significant impact in the computational effort. In particular, the accuracy in the prediction of the mass flow rate improves around 5% when using the compressible flow approach. Other flow characteristics such as the momentum flux and the effective outlet velocity, which are key inputs for spray models, also show a significant improvement in accuracy.

ACKNOWLEDGEMENTS.

This work was partly sponsored by "*Ministerio de Economía y Competitividad*", of the Spanish Government, in the frame of the Project "*Estudio de la interacción chorro-pared en condiciones realistas de motor*", Reference *TRA2015-67679-c2-1-R*. The authors would like also to thank the computer resources, technical expertise and assistance provided by Universidad de Valencia in the use of the supercomputer "*Tirant*". Mr. Jaramillo's Thesis is funded by "Conselleria d'Educació, Cultura i Esports" of Generalitat Valenciana in the frame of the program "Programa VALI+D para investigadores en formación, Reference ACIF/2015/040.

References

[1] M. Weilenmann, P. Soltic, C. Saxer, A. M. Forss, and N. Heeb, "Regulated and nonregulated diesel and gasoline cold start emissions at different temperatures," *Atmos. Environ.*, vol. 39, pp. 2433–2441, 2005.

[2] G. Archer, "Briefing: Particle emissions from petrol cars," *Transp. Environ.*, no. November, pp. 1–4, 2013.

[3] V. Bermúdez, J. M. Lujan, H. Climent, and D. Campos, "Assessment of pollutants emission and aftertreatment efficiency in a GTDi engine including

cooled LP-EGR system under different steady-state operating conditions," *Appl. Energy*, vol. 158, pp. 459–473, 2015.

[4] B. Guan, R. Zhan, H. Lin, and Z. Huang, "Review of state of the art technologies of selective catalytic reduction of NOx from diesel engine exhaust," *Appl. Therm. Eng.*, vol. 66, no. 1–2, pp. 395–414, 2014.

[5] D. S. Kim and C. S. Lee, "Improved emission characteristics of HCCI engine by various premixed fuels and cooled EGR," *Fuel*, vol. 85, no. 5–6, pp. 695–704, 2006.

[6] C. A. Idicheria and L. M. Pickett, "Effect of EGR on diesel premixed-burn equivalence ratio," *Proc. Combust. Inst.*, vol. 31, no. 2, pp. 2931–2938, 2007.

[7] X. Lu, D. Han, and Z. Huang, "Fuel design and management for the control of advanced compression-ignition combustion modes," *Prog. Energy Combust. Sci.*, vol. 37, no. 6, pp. 741–783, 2011.

[8] J. Benajes, R. Novella, D. De Lima, and P. Tribotté, "Analysis of combustion concepts in a newly designed two-stroke high-speed direct injection compression ignition engine," *Int. J. Engine Res.*, vol. 16, no. 1, pp. 52–67, 2014.

[9] T. Kato, T. Koyama, K. Sasaki, and K. K. Mori, "Common Rail Fuel Injection System for Improvement of Engine Performance on Heavy Duty Diesel Engine," *SAE Pap. 980806*, no. 724, 1998.

[10] F. J. Salvador, A. H. Plazas, J. Gimeno, and M. Carreres, "Complete modelling of a piezo actuator last-generation injector for diesel injection systems," *Int. J. Engine Res.*, vol. 15, no. 1, pp. 3–19, Jan. 2014.

[11] M. Gavaises and A. Andriotis, “Cavitation Inside Multi-hole Injectors for Large Diesel Engines and Its Effect on the Near-nozzle Spray Structure,” *SAE Tech. Pap. 2006-01-1114*, vol. 2006, no. 724, 2006.

[12] L. C. Ganippa, G. Bark, S. Andersson, and J. Chomiak, “Comparison of cavitation phenomena in transparent scaled-up single-hole Diesel nozzles,” in *Symposium on Cavitation*, 2001, pp. 1–9.

[13] Y. Zhang, S. Li, B. Zheng, J. Wu, and B. Xu, “Quantitative observation on breakup of superheated liquid jet using transparent slit nozzle,” *Exp. Therm. Fluid Sci.*, vol. 63, pp. 84–90, 2015.

[14] R. Payri, F. J. Salvador, J. Gimeno, and O. Venegas, “Study of cavitation phenomenon using different fuels in a transparent nozzle by hydraulic characterization and visualization,” *Exp. Therm. Fluid Sci.*, vol. 44, pp. 235–244, 2013.

[15] B. Mohan, W. Yang, and S. K. Chou, “Cavitation in Injector Nozzle Holes - A Parametric Study,” *Eng. Appl. Comput. Fluid Mech.*, vol. 8, no. 1, pp. 70–81, 2014.

[16] C. Badock, R. Wirth, A. Fath, and A. Leipertz, “Investigation of cavitation in real size diesel injection nozzles,” *Int. J. Heat Fluid Flow*, vol. 20, no. 5, pp. 538–544, 1999.

[17] G. Jiang, Y. Zhang, H. Wen, and G. Xiao, “Study of the generated density of cavitation inside diesel nozzle using different fuels and nozzles,” *Energy Convers. Manag.*, vol. 103, pp. 208–217, 2015.

[18] N. Mitroglou, M. McLorn, M. Gavaises, C. Soteriou, and M. Winterbourne, “Instantaneous and ensemble average cavitation structures in Diesel micro-channel flow orifices,” *Fuel*, vol. 116, pp. 736–742, 2014.

[19] S. Som, A. I. Ramírez, D. E. Longman, and S. K. Aggarwal, “Effect of nozzle orifice geometry on spray, combustion, and emission characteristics under diesel engine conditions,” *Fuel*, vol. 90, no. 3, pp. 1267–1276, 2011.

[20] F. J. Salvador, M. Carreres, D. Jaramillo, and J. Martínez-López, “Comparison of microsac and VCO diesel injector nozzles in terms of internal nozzle flow characteristics,” *Energy Convers. Manag.*, vol. 103, pp. 284–299, 2015.

[21] S. Molina, F. J. Salvador, M. Carreres, and D. Jaramillo, “A computational investigation on the influence of the use of elliptical orifices on the inner nozzle flow and cavitation development in diesel injector nozzles,” *Energy Convers. Manag.*, vol. 79, pp. 114–127, 2014.

[22] F. J. Salvador, J. Martínez-López, J. V. Romero, and M. D. Roselló, “Computational study of the cavitation phenomenon and its interaction with the turbulence developed in diesel injector nozzles by Large Eddy Simulation (LES),” *Math. Comput. Model.*, vol. 57, no. 7–8, pp. 1656–1662, 2013.

[23] M. Battistoni and C. N. Grimaldi, “Numerical analysis of injector flow and spray characteristics from diesel injectors using fossil and biodiesel fuels,” *Appl. Energy*, vol. 97, pp. 656–666, 2012.

[24] F. J. Salvador, S. Ruiz, J. Gimeno, and J. De la Morena, “Estimation of a suitable Schmidt number range in diesel sprays at high injection pressure,” *Int. J. Therm.*

Sci., vol. 50, no. 9, pp. 1790–1798, 2011.

[25] F. J. Salvador, J. V. Romero, M. D. Roselló, and D. Jaramillo, "Numerical simulation of primary atomization in diesel spray at low injection pressure," *J. Comput. Appl. Math.*, vol. 291, pp. 94–102, 2015.

[26] K. H. Kwak, D. Jung, and C. Borgnakke, "Enhanced Spray and Evaporation Model with Multi-Fuel Mixtures for Direct Injection Internal Combustion Engines," *Int. J. Engine Res.*, vol. 15, no. 4, p. 1468087413495203-, 2013.

[27] F. J. Salvador, S. Ruiz, J. M. Salavert, and J. De la Morena, "Consequences of using biodiesel on the injection and air-fuel mixing processes in diesel engines," *Proc. Inst. Mech. Eng. Part D J. Automob. Eng.*, vol. 227, no. 8, pp. 1130–1141, 2013.

[28] S. Som, D. E. Longman, A. I. Ramírez, and S. K. Aggarwal, "A comparison of injector flow and spray characteristics of biodiesel with petrodiesel," *Fuel*, vol. 89, pp. 4014–4024, 2010.

[29] O. A. Kuti, J. Zhu, K. Nishida, X. Wang, and Z. Huang, "Characterization of spray and combustion processes of biodiesel fuel injected by diesel engine common rail system," *Fuel*, vol. 104, pp. 838–846, 2013.

[30] J. M. Lujan, B. Tormos, F. J. Salvador, and K. Gargar, "Comparative analysis of a DI diesel engine fuelled with biodiesel blends during the European MVEG-A cycle: Preliminary study (I)," *Biomass and Bioenergy*, vol. 33, no. 6–7, pp. 941–947, 2009.

[31] F. J. Salvador, J. Gimeno, J. De la Morena, and M. Carreres, "Using one-

dimensional modeling to analyze the influence of the use of biodiesels on the dynamic behavior of solenoid-operated injectors in common rail systems: Results of the simulations and discussion," *Energy Convers. Manag.*, vol. 54, no. 1, pp. 122–132, 2012.

[32] P. Tinprabath, C. Hespel, S. Chanchaona, and F. Foucher, "Influence of biodiesel and diesel fuel blends on the injection rate under cold conditions," *Fuel*, vol. 144, pp. 80–89, 2015.

[33] R. Payri, F. J. Salvador, J. Gimeno, and G. Bracho, "Effect of fuel properties on diesel spray development in extreme cold conditions," *Proc. Inst. Mech. Eng. Part D, J. Automob. Eng.*, vol. 222, no. 9, pp. 1743–1753, 2008.

[34] R. Payri, F. J. Salvador, J. Gimeno, and G. Bracho, "Understanding Diesel Injection Characteristics in Winter Conditions," *SAE Tech. Pap. 2009-01-0836*, 2009.

[35] G. Strotos, P. Koukouvinis, A. Theodorakakos, M. Gavaises, and G. Bergeles, "Transient heating effects in high pressure Diesel injector nozzles," *Int. J. Heat Fluid Flow*, vol. 51, pp. 257–267, 2015.

[36] A. Theodorakakos, G. Strotos, N. Mitroglou, C. Atkin, and M. Gavaises, "Friction-induced heating in nozzle hole micro-channels under extreme fuel pressurisation," *Fuel*, vol. 123, no. x, pp. 143–150, 2014.

[37] P. Koukouvinis, M. Gavaises, J. Li, and L. Wang, "Large Eddy Simulation of Diesel injector including cavitation effects and correlation to erosion damage," *Fuel*, vol. 175, pp. 26–39, 2016.

[38] I. H. Sezal, S. J. Schmidt, G. H. Schnerr, M. Thalhamer, and M. Förster, "Shock and wave dynamics in cavitating compressible liquid flows in injection nozzles," *Shock Waves*, vol. 19, no. 1, pp. 49–58, 2009.

[39] F. Örley, S. Hickel, S. J. Schmidt, and N. A. Adams, "Large-Eddy Simulation of turbulent, cavitating fuel flow inside a 9-hole Diesel injector including needle movement," *Int. J. Engine Res.*, vol. 656, p. 12097, Apr. 2016.

[40] A. Mulemane, S. Subramaniyam, P. Lu, J.-S. J.-S. Han, M.-C. M.-C. Lai, R. Poola, P.-H. Liu, J.-S. J.-S. Han, M.-C. M.-C. Lai, and R. Poola, "Comparing cavitation in Diesel injectors based on different modeling approaches," *SAE Tech. Pap. 2004-01-0027*, 2004.

[41] F. J. Salvador, M. Carreres, D. Jaramillo, and J. Martínez-López, "Analysis of the combined effect of hydrogrinding process and inclination angle on hydraulic performance of diesel injection nozzles," *Energy Convers. Manag.*, vol. 105, pp. 1352–1365, 2015.

[42] V. Macian, V. Bermúdez, R. Payri, and J. Gimeno, "New technique for determination of internal geometry of a Diesel nozzle with the use of silicone methodology," *Exp. Tech.*, vol. 27, no. April, pp. 39–43, 2003.

[43] Z. He, G. Guo, X. Tao, W. Zhong, X. Leng, and Q. Wang, "Study of the effect of nozzle hole shape on internal flow and spray characteristics," *Int. Commun. Heat Mass Transf.*, vol. 71, pp. 1–8, 2016.

[44] F. Payri, V. Bermúdez, R. Payri, and F. J. Salvador, "The influence of cavitation on the internal flow and the spray characteristics in diesel injection nozzles,"

Fuel, vol. 83, no. 4–5, pp. 419–431, 2004.

[45] J. M. Desantes, F. J. Salvador, M. Carreres, and D. Jaramillo, "Experimental Characterization of the Thermodynamic Properties of Diesel Fuels Over a Wide Range of Pressures and Temperatures," *SAE Int. J. Fuels Lubr.*, vol. 8, no. 1, pp. 2015-01–0951, 2015.

[46] W. Bosch, "The Fuel Rate Indicator: a New Measuring Instrument for Display of the Characteristics of Individual Injection," *SAE Pap. 660749*, 1966.

[47] R. Payri, F. J. Salvador, J. Gimeno, and G. Bracho, "A new methodology for correcting the signal cumulative phenomenon on injection rate measurements," *Exp. Tech.*, vol. 32, no. February, pp. 46–49, 2008.

[48] R. Payri, J. M. Garcia-Oliver, F. J. Salvador, and J. Gimeno, "Using spray momentum flux measurements to understand the influence of diesel nozzle geometry on spray characteristics," *Fuel*, vol. 84, no. 5, pp. 551–561, 2005.

[49] ANSYS ® Fluent ® is a trademark of ANSYS Inc.

[50] F. J. Salvador, S. Hoyas, R. Novella, and J. Martínez-López, "Numerical simulation and extended validation of two-phase compressible flow in diesel injector nozzles," *Proc. Inst. Mech. Eng. Part D J. Automob. Eng.*, vol. 225, no. 4, pp. 545–563, 2011.

[51] A. K. Lichtarowicz, R. K. Duggins, and E. Markland, "Discharge coefficients for incompressible non- cavitating flow through long orifices," *J. Mech. Eng. Sci.*, vol. 7, no. 2, pp. 210–219, 1965.

[52] R. Payri, F. J. Salvador, J. Gimeno, and J. De la Morena, “Study of cavitation phenomena based on a technique for visualizing bubbles in a liquid pressurized chamber,” *Int. J. Heat Fluid Flow*, vol. 30, no. 4, pp. 768–777, 2009.

[53] R. Payri, F. J. Salvador, J. Gimeno, and A. Garcia, “Flow regime effects over non-cavitating Diesel injection nozzles,” *J. Automob. Eng.*, vol. 226, pp. 133–144, 2011.

[54] F. J. Salvador, M. Carreres, D. Jaramillo, and J. Martínez-lópez, “Analysis of the combined effect of hydrogrinding process and inclination angle on hydraulic performance of diesel injection nozzles,” *Energy Convers. Manag.*, vol. 105, pp. 1352–1365, 2015.

Tables

Orifice	Ra [μm]	Rb [μm]	Di [μm]	Dm [μm]	Do [μm]	k-factor [-]	Length [μm]
1	23	13	141	129	123	1.7	703
2	27	23	145	131	127	1.8	704
3	20	24	145	132	126	1.9	707
4	36	20	141	128	122	1.8	726
5	38	28	145	130	123	2.2	737

Mean Values	**29±8**	**22 ±6**	**143 ±2.3**	**130 ±1.4**	**124 ±2.2**	**1.9 ±0.2**	**715 ±15**

Table 1. Nozzle geometric characteristics

Injection Pressures [MPa]	**Back-Pressures [MPa]**								
30	**0.5**	**1**	**3**	**5**	**7**	**9**	**11**	**13**	**15**
80		**1**	**3**	**5**	**7**	**9**	**11**	**13**	**15**
130		**1**	**3**	**5**	**7**	**9**	**11**	**13**	**15**
180		**1**	**3**	**5**	**7**	**9**	**11**	**13**	**15**
250		**1**	**3**	**5**	**7**	**9**	**11**	**13**	**15**

Table 2. Text matrix for mass flow rate measurements.

Injection Pressures [MPa]	**Back-Pressures [MPa]**				
30	**0.5**	**1**	**3**	**5**	**7**
80		**1**	**3**	**5**	**7**
130		**1**	**3**	**5**	**7**
180		**1**	**3**	**5**	**7**
250		**1**	**3**	**5**	**7**

Table 3. Text matrix for Momentum flux measurements.

Figure captions.

Figure 1. Nozzle geometry determination.

Figure 2. Winter diesel properties as a function of pressure and temperature.

Figure 3. Mass flow rates at P_{inj}= 180 MPa and all back-pressures.

Figure 4. Momentum flux at P_{inj}= 180 MPa and all back-pressures.

Figure 5. Details of nozzle mesh.

Figure 6. Mesh sensitibity study for first and second order schemes.

Figure 7. Fields of density and viscosity obtained from CFD simulations (compressible approach) for an injection pressure of 250 MPa and backpressure of 5 MPa

Figure 8: Fields of pressure and velocity for compressible and incompressible solutions. P_{inj} = 250 MPa, P_b = 5 MPa.

Figure 9. Experimental mass flow results compared to those of CFD calculations for incompressible and compressible approaches.

Figure 10. Experimental discharge coefficient results compared to those of CFD calculations for incompressible and compressible approaches.

Figure 11. Experimental effective injection velocity results compared to those of CFD calculations for incompressible and compressible approaches.

Figure 12. Mass flow deviation among experimental and modelled (incompressible and compressible approaches)

Figure 13. Velocity deviation among experimental and modelled (incompressible and compressible approaches)

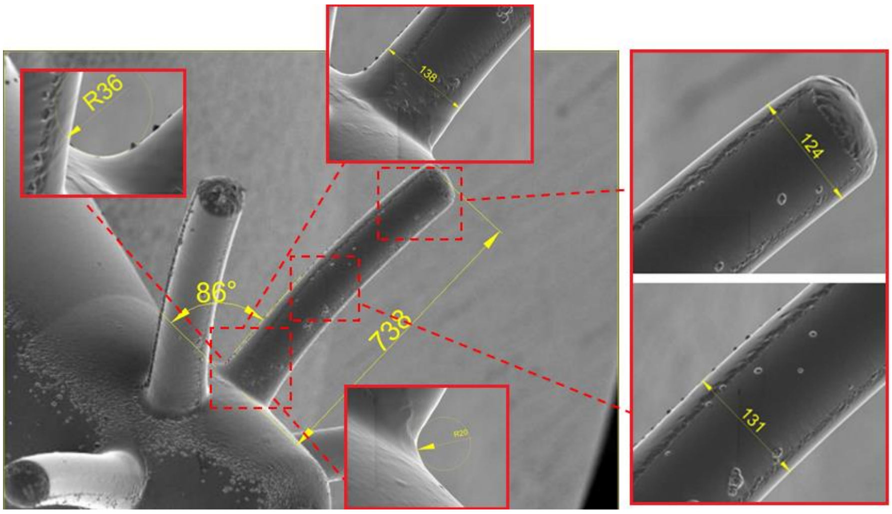

Figure 1. Nozzle geometry determination.

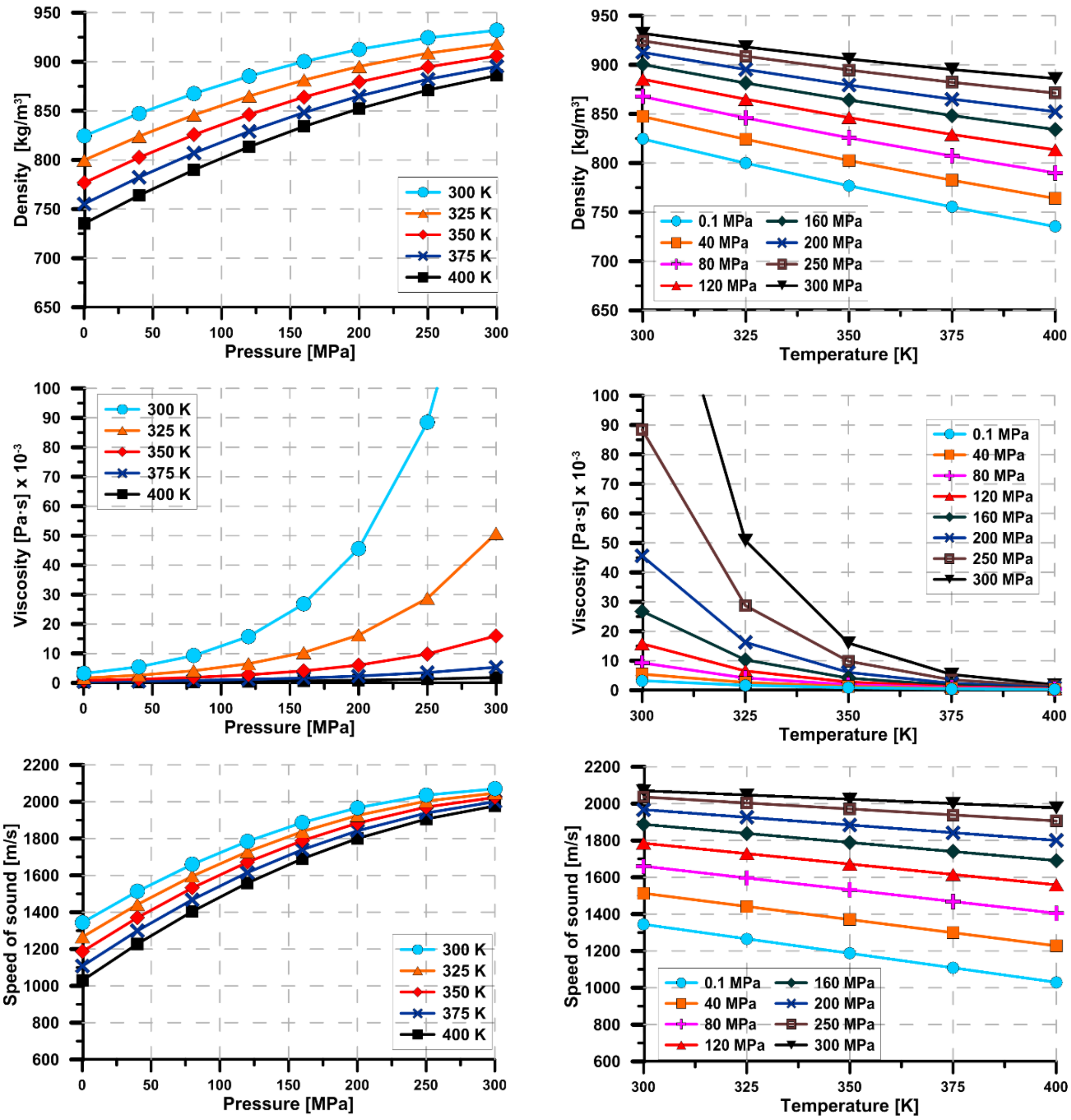

Figure 2. Winter diesel properties as a function of pressure and temperature.

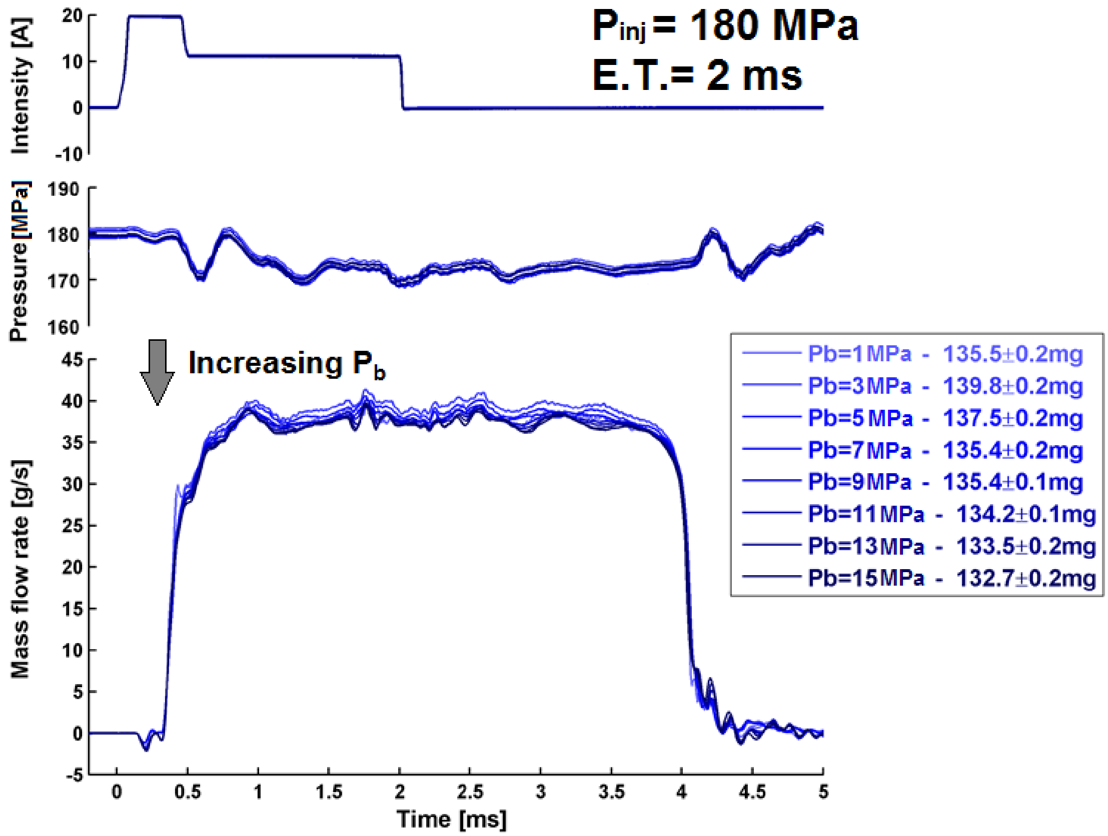

Figure 3. Mass flow rates at P_{inj}= 180 MPa and all back-pressures.

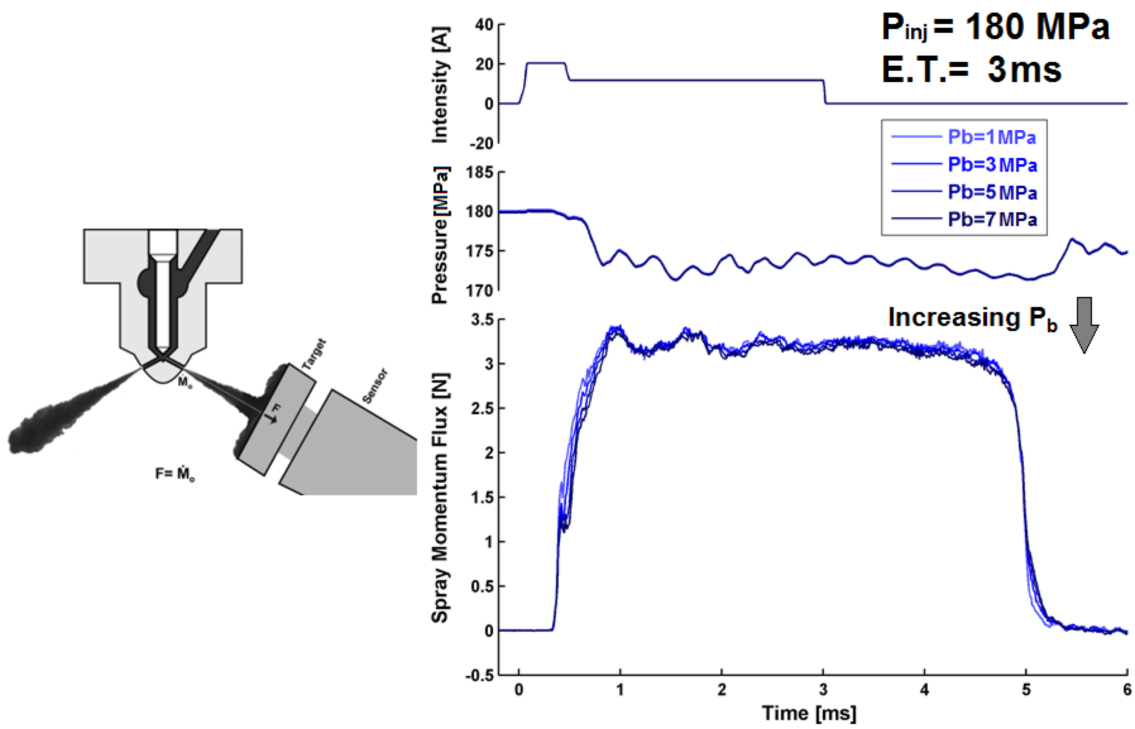

Figure 4. Momentum flux at P_{inj}= 180 MPa and all back-pressures.

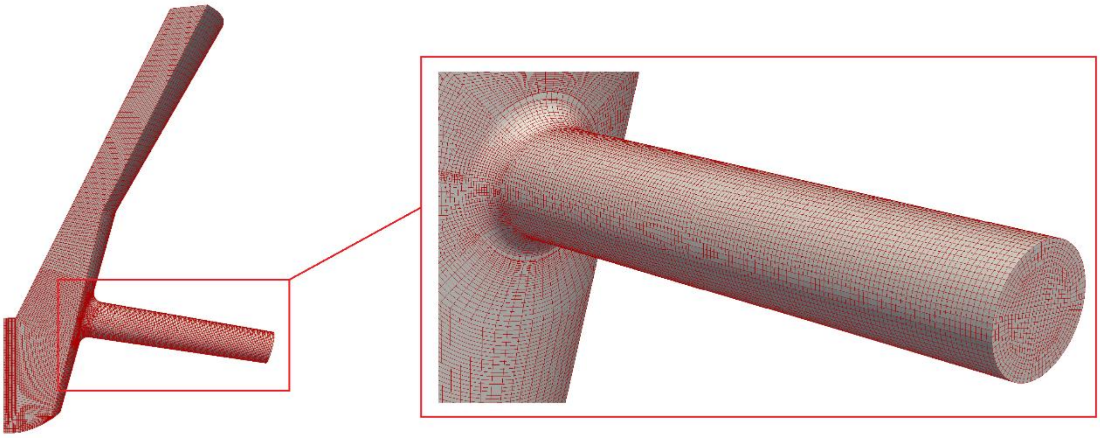

Figure 5. Details of nozzle mesh.

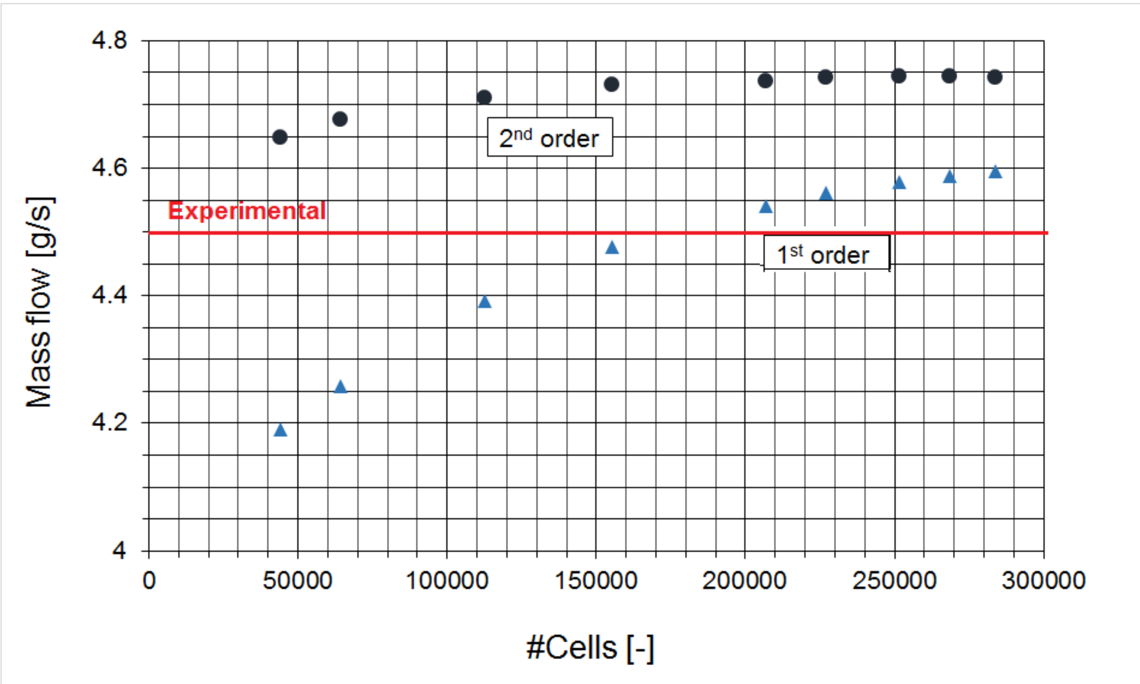

Figure 6. Mesh sensitibity study for first and second order schemes. P_{inj} = 130 MPa, P_b=5 MPa

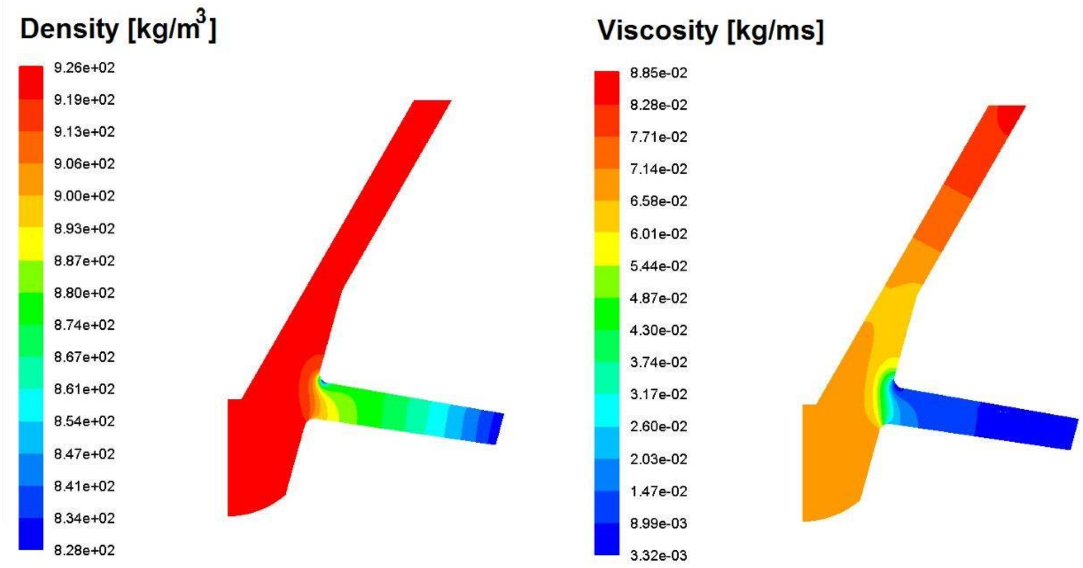

Figure 7. Fields of density and viscosity obtained from CFD simulations (compressible approach) for an injection pressure of 250 MPa and backpressure of 5 MPa

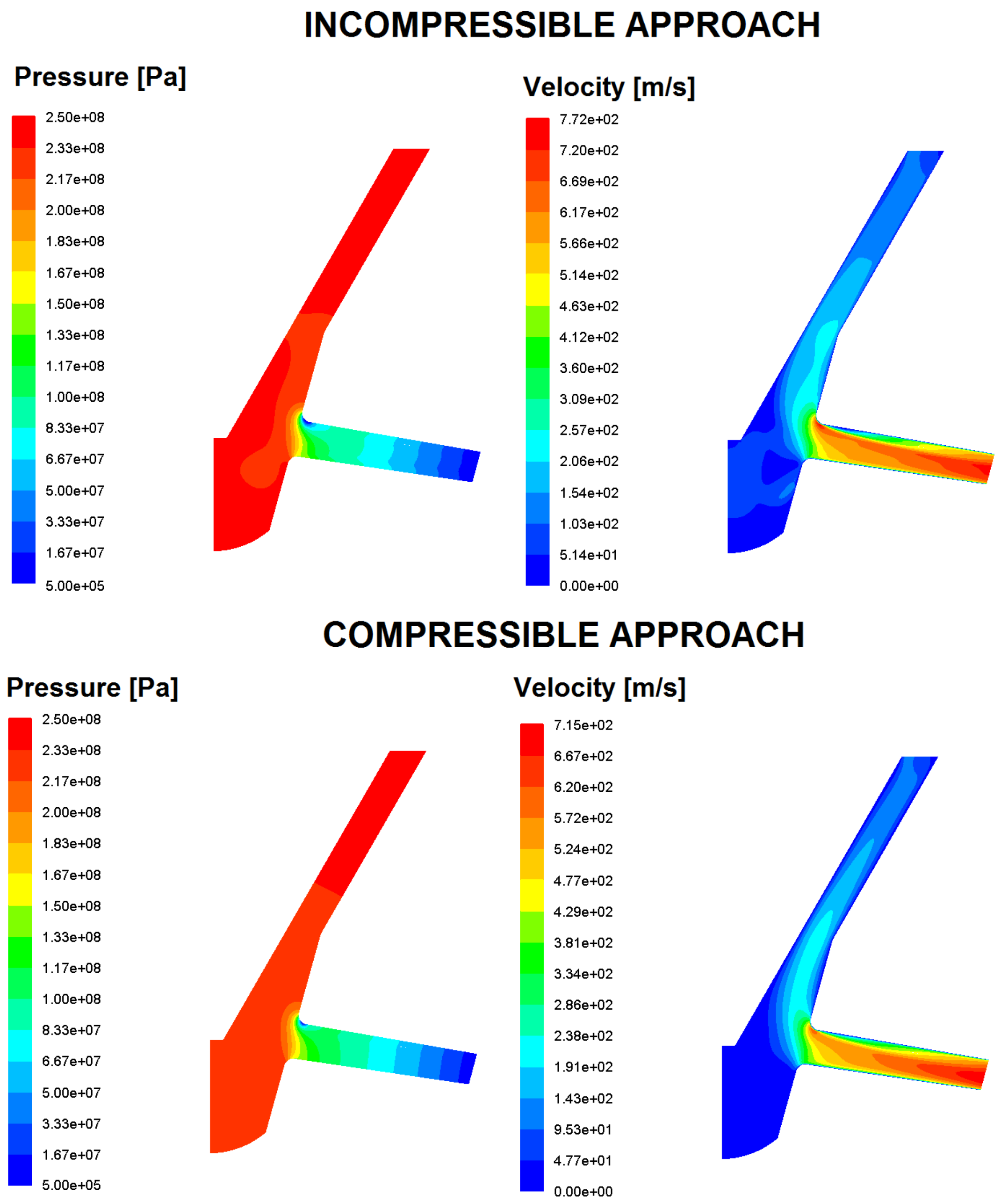

Figure 8: Fields of pressure and velocity for compressible and incompressible solutions. P_{inj} = 250 MPa, P_b = 5 MPa.

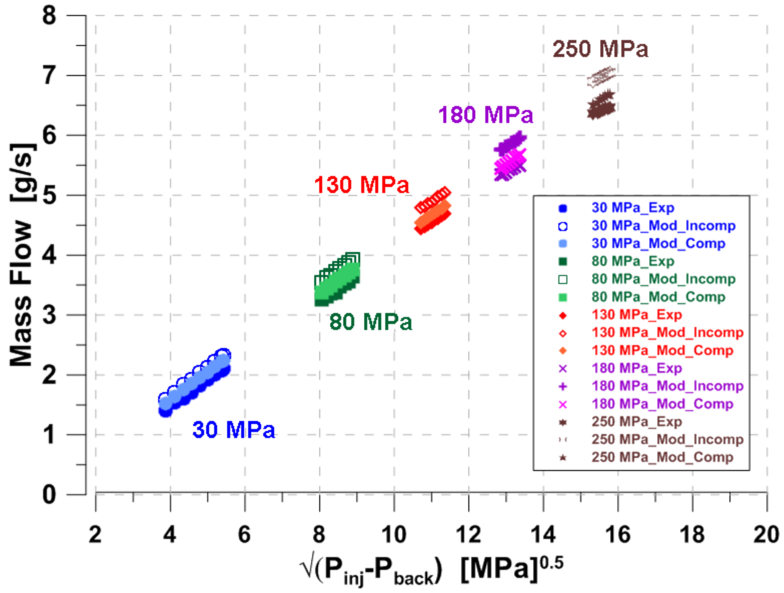

Figure 9. Experimental mass flow results compared to those of CFD calculations for incompressible and compressible approaches.

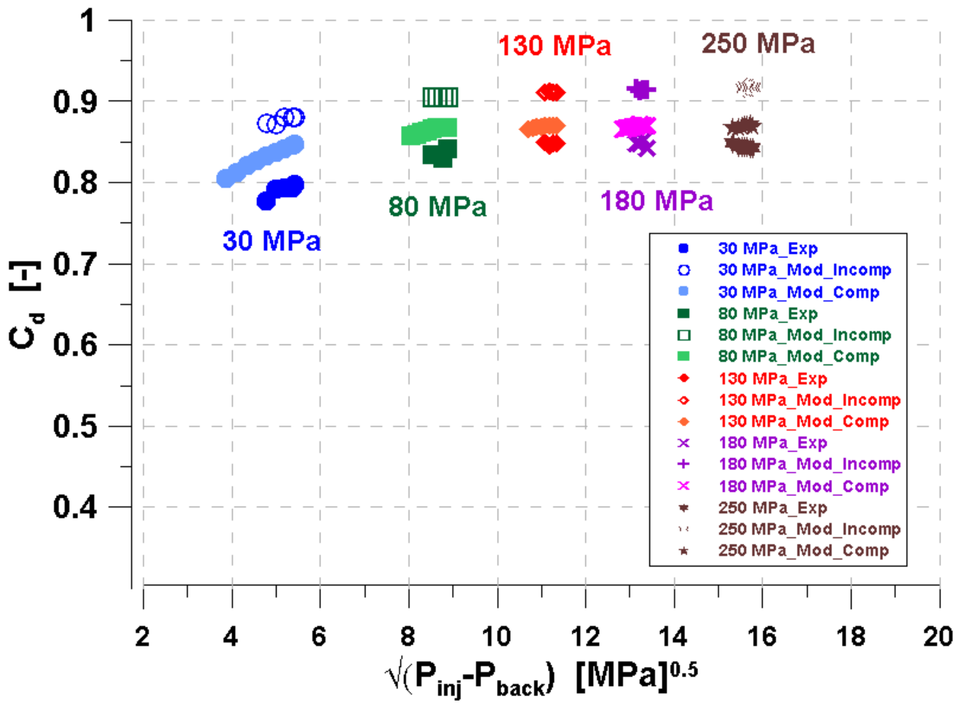

Figure 10. Experimental discharge coefficient results compared to those of CFD calculations for incompressible and compressible approaches.

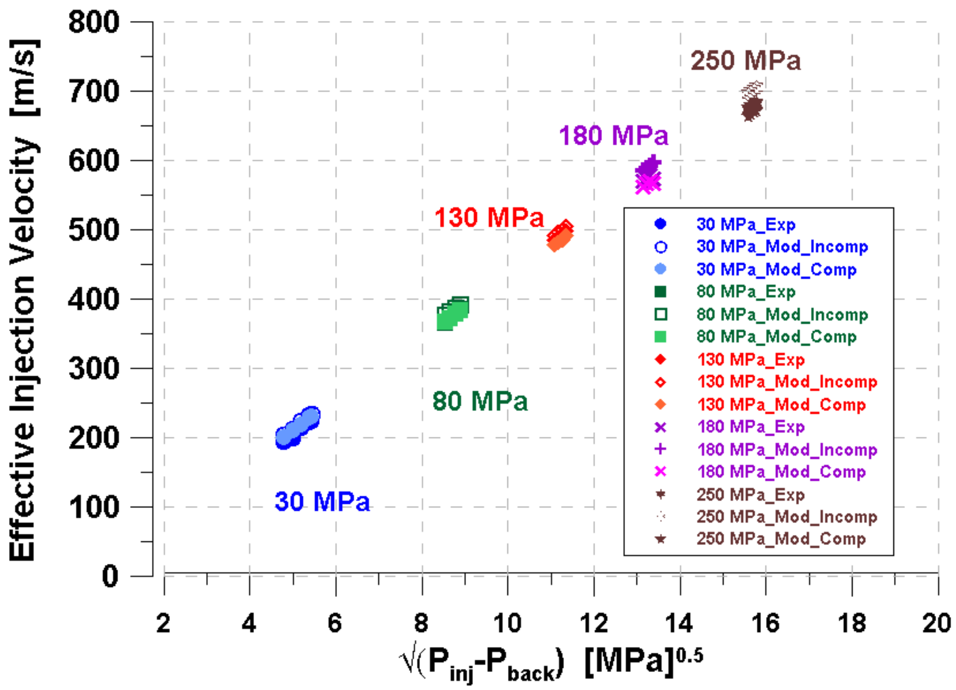

Figure 11. Experimental effective injection velocity results compared to those of CFD calculations for incompressible and compressible approaches.

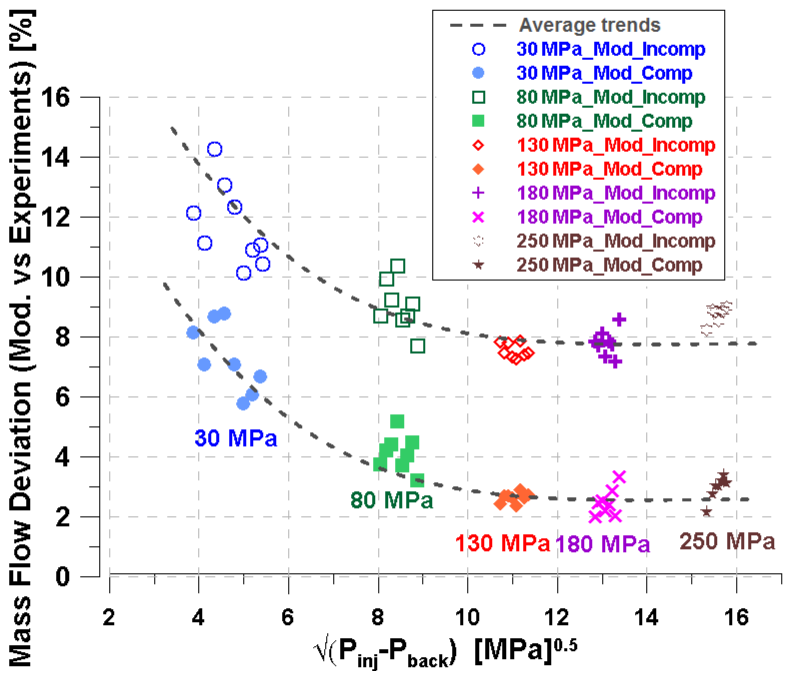

Figure 12. Mass flow deviation among experimental and modelled (incompressible and compressible approaches)

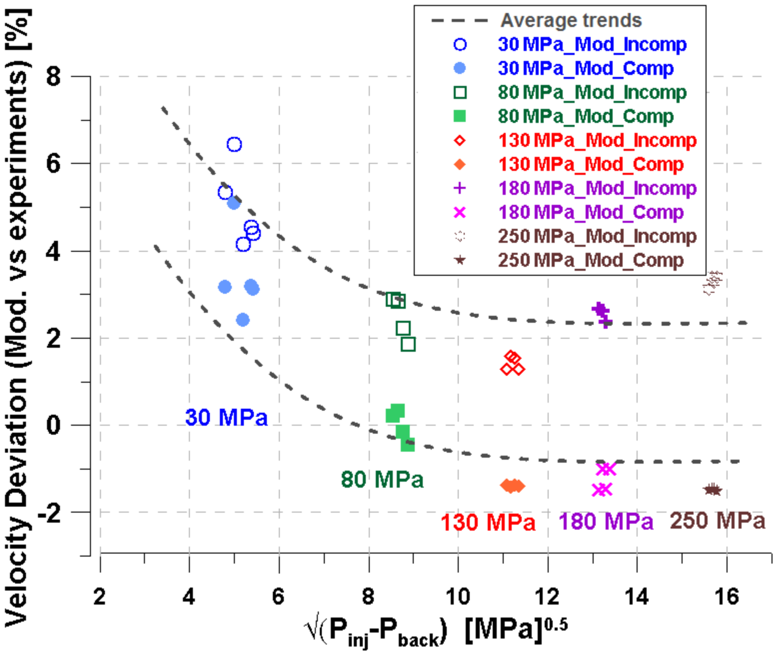

Figure 13. Velocity deviation among experimental and modelled (incompressible and compressible approaches)